

X-ray computed tomography to observe the presence of water in macropores of cementitious materials

Emanuele Rossi^{1,*}, Susanna Governo¹, Mahdiah Shakoorioskooie², Qianru Zhan², Shishir Mundra¹, David Mannes², Anders Kaestner², Ueli Angst¹

¹ Institute for Building Materials, ETH Zurich, Switzerland

² Laboratory for Neutron Scattering and Imaging (LNS), Paul Scherrer Institut, 5232 Villigen, Switzerland

Received: 25 November 2023 / Accepted: 18 March 2024 / Published online: 09 April 2024

© The Author(s) 2024. This article is published with open access and licensed under a Creative Commons Attribution 4.0 International License.

Abstract

Corrosion of steel reinforcement in concrete is a common degradation mechanism occurring in infrastructures worldwide. Even though extensive research has been conducted over the last decades to accurately predict the influence of steel corrosion on concrete durability, a comprehensive understanding of several micro-scale processes simultaneously involved in the corrosion mechanism is still lacking. The application of X-ray Computed Tomography (X-ray CT) can contribute to elucidate these processes, since this technique allows observing the internal status of specimens non-destructively, over time, and with a spatial resolution in the range of μm . Nevertheless, the relatively low sensitivity of light elements (e.g., hydrogen and oxygen) to X-ray CT may hinder the observation of solution within the cementitious matrix. This consideration is discussed in this letter. The results of this study show that the detection of solution in macropores (e.g., air voids) through X-ray CT is not limited by the relatively low attenuation coefficient of the fluid per se, but more by the spatial resolution at which acquisitions are performed and by the dimensions of the porous volume where solution penetrates. The observations reported in this letter may open several opportunities to further study the influence of the moisture conditions of air voids on several degradation mechanisms of reinforced cementitious materials (e.g., steel corrosion, freeze-thaw damage), which have been rarely investigated with X-ray CT according to the literature. The application of these findings could significantly deepen the understanding of several micro-scale processes that affect the durability of reinforced cementitious materials which still need to be elucidated, as further discussed in the present letter.

Keywords: X-ray Computed Tomography; Corrosion; Steel; Concrete

1 Introduction

The construction materials industry is facing several challenges to reduce its environmental impact, which currently accounts for more than 8% of the total CO₂ emissions due to anthropogenic activities [1]. Both scientific and industrial partners are working jointly on possible solutions to reduce the environmental footprint of the sector [2]. Among them, exploiting the service life of the built environment to its ultimate state would significantly lower the consumption of concrete, as well as enormously reduce the human, materials, and monetary resources related to the direct and indirect costs pertaining to their end-of-life management. However, service life models that can accurately predict the status of the construction materials over time and, therefore, of the built environment made of them, are still lacking. To be accurate, service life models of reinforced concrete structures must consider the different degradation mechanisms occurring at various time and dimensional scales inside the construction materials, and how these mechanisms influence the onsite properties of

the infrastructure. Among the different degradation mechanisms, corrosion of the steel reinforcement in concrete is the most common cause of degradation of reinforced concrete structures worldwide [3], which may lead to catastrophic structural failures if not properly prevented [4]. As a matter of fact, corrosion of reinforced concrete has been widely studied over the last decades through countless methodologies and techniques [5]. Nevertheless, the heterogeneity of the material, the complexity of the microscopic physiochemical processes simultaneously occurring in corroding reinforced concrete structures, and their multi-scale effects on the material durability, still hinder the formulation of theories supported by experimental evidence that could elucidate fundamental aspects of the whole multi-scale corrosion mechanism. Hence, substantial progress is still needed in terms of the scientific understanding of all the coupled properties and mechanisms relevant to corrosion and corrosion-related damages [4]. Recent advances in the field of X-Ray Computed Tomography (X-ray CT) have enabled us to better understand the process of steel corrosion in the context of porous

*Corresponding authors: Emanuele Rossi, e-mail: emanuele.rossi@ifb.baug.ethz.ch

media (in particular, the case of reinforced concrete) and its consequences on their durability. X-ray CT allows us to observe multi-scale processes and degradation mechanisms in-situ at specific points in time within the concrete matrix, thereby overcoming the opacity of concrete as well as avoiding any specimen manipulation during the preparation for destructive analysis. For these reasons, the number of studies in which X-ray CT has been used to investigate the corrosion of steel in concrete has been considerably growing over the last two decades, as shown in Figure 1. Nevertheless, the relatively low number of published studies (32 in total, as of now) suggests that the use of X-ray CT to monitor and analyze steel reinforcement corrosion in concrete is still in its infancy, and of the full potential of this technique may not be completely explored nor exploited yet.

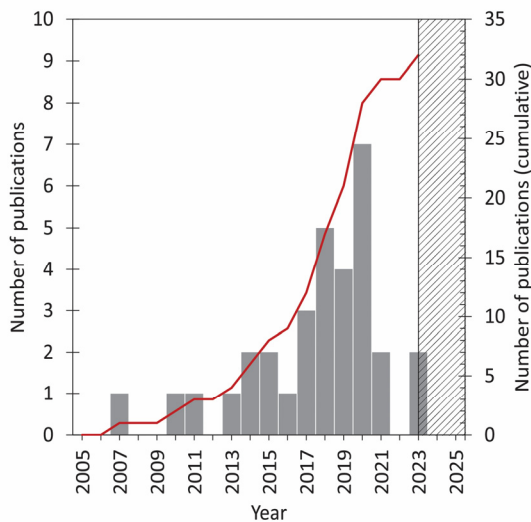


Figure 1. The number of publications about the application of X-ray CT to study corrosion of steel in concrete over time (available on Scopus and Google Scholar). The red line corresponds to the cumulative curve.

The working principles behind X-ray CT have been widely described in the literature [6-9], as well as its application to study the properties of cementitious materials [10] and of the steel reinforcement corrosion therein embedded [11]. Hence, the basics of X-ray CT will be only briefly touched upon in this letter. At the same time, considerations about some of the unexploited potential of X-ray CT will be elaborated, that is, the possibility of observing the presence of solution in the macroscopic porous network of cementitious materials.

2 Basics of X-ray CT to study corrosion of steel in concrete

X-ray CT allows to three-dimensionally image the internal composition of a specimen, and a typical tomography setup

comprises three main parts: the source of X-rays, the detector measuring the X-rays after being attenuated by the sample, and the sample itself (Figure 2).

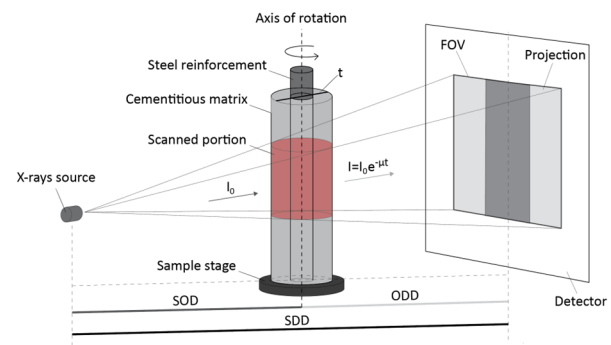


Figure 2. Schematic representation of a typical X-ray CT setup (SOD=source-object distance; ODD=object-detector distance; SDD=source-detector distance; t =specimen thickness; μ =linear attenuation coefficient; FOV=field of view).

The sample is positioned between the source and the detector, and the sample stage is allowed to rotate by 360° during the exposure to X-rays. As a result, the output of a full X-ray CT acquisition is a set of radiographs (i.e., projections) taken at different angles. These projections are then transformed into a 3D volume through a mathematical reconstruction process [12]. Most of the reconstruction algorithms rely on Beer-Lambert's law, which relates the intensity of the incident X-ray beam generated from the source to the intensity of the X-ray beam that emerges from the sample after exposure according to Equation (1):

$$I(t) = I_0 e^{-\mu t} \quad (1)$$

where I_0 is the initial X-ray beam intensity incident on the sample, I is the X-ray beam attenuated by the sample (a fraction of the intensity of the incident beam), μ is the linear attenuation coefficient of the exposed material (cm^{-1}) and t is the thickness of the exposed specimen (cm).

The linear attenuation coefficient of a material mainly depends on its density and atomic number, and it varies as a function of the photon energy that generates polychromatic X-rays as typically employed in laboratory setups. This dependency is clearly visible in Figure 3a, where linear attenuation coefficients of the phases typically found in reinforced concrete specimens, namely water, dry air, calcium silicate hydrates (C-S-H), calcium hydroxide (CH), aggregates (such as sand grains) and iron are reported [13].

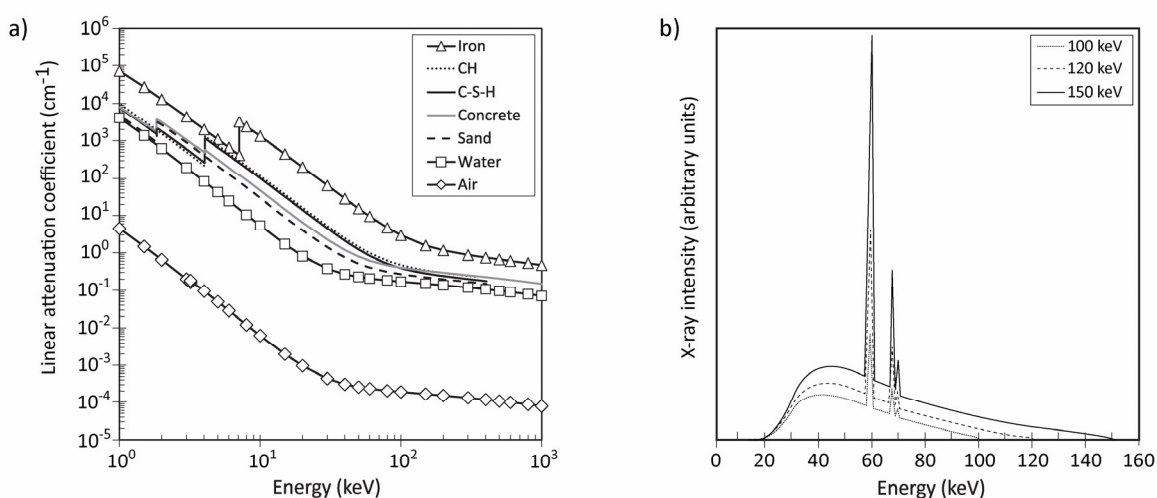


Figure 3. a) Linear attenuation coefficients of the phases typically found in reinforced concrete specimens as a function of the source electron acceleration voltage. Data obtained from NIST Standard Reference database 126 [13]; b) schematic representation of a filtered X-ray spectrum generated from a tungsten target (as typically conducted in laboratory setups) with varying electron acceleration voltages at the source (data obtained from SpekCalc [14-16]).

The different linear attenuation coefficients of the internal components of the specimen allow to differentiate the phases present within the scanned volume. X-rays are locally attenuated by matter depending on its chemical composition, and this attenuation is eventually translated into a grayscale value (GSV) characteristic to the respective 2D pixel (or 3D voxel) of the reconstructed images. In this way, a higher difference in linear attenuation coefficients results in a higher likelihood to distinguish and segment the respective phases. The accuracy of this segmentation is influenced by the different photon energies at the X-ray source and through the specimen, which decreases depending on the specimen thickness and composition [8]. The X-ray beam incident on the specimen is indeed a spectrum due to the polychromatic nature of X-rays, as visible in Figure 3b [14-16]. Due to the change of photon energy through the specimen during the acquisition, similar phases may interact with different energy of X-ray depending on, for instance, their position within the specimen volume. Since the linear attenuation coefficient of matter depends on the energy of the incident photons, identical phases interacting with an X-ray beam spectrum may have a different GSV in the output images, which may influence the accuracy of their segmentation.

Another key factor to distinguish different components within one specimen is the spatial resolution of the acquired images. The spatial resolution can indeed be defined as the optical quantity that indicates the ability of an imaging setup to separate close objects [10], and it is inversely proportional to the voxel size of one image. The spot size of the X-ray source, the resolution of the detection system (i.e., the geometric size of a pixel on the detector) and the magnification at which the acquisitions are performed influence the resolution of the output images [8]. The magnification depends on the source-to-object (SOD) and object-to-detector (ODD) distances (Figure 2), which are directly related to the thickness and geometry of the analyzed specimen. In acquisitions where the sample is positioned vertically between the X-ray source and

the detector (Figure 2), the thinner the specimen the shorter the SOD (at which the specimen can be positioned and, therefore, the higher the resolution [9]).

While some components of reinforced concrete specimens can be generally distinguished using typical X-ray CT setups (like iron and air, for instance), Figure 3a also clearly shows that the cement hydration products (e.g., C-S-H and CH) have very similar linear attenuation coefficients regardless of the energy to which they are exposed. Hence, while the bulk cementitious matrix can be clearly detected, an accurate micro-scale distinction between its different cementitious hydration products cannot be usually performed. The detection of the different hydration products is also hindered by the spatial resolution of the X-ray CT acquisitions generally performed for reinforced cementitious specimens, as further discussed later in this manuscript. The linear attenuation coefficients of CH and C-S-H are also very similar to that of sand grains (Figure 3), which does not usually allow to clearly distinguish siliceous aggregates within the cementitious matrix. Besides increasing the signal-to-noise (SNR) ratio of the acquisition (which is described later in this manuscript), their distinction may be possible when aggregates are relatively coarse and, therefore, with a large interfacial zone (ITZ). The boundaries between the aggregate particles and the surrounding cementitious matrix define the aggregates shape and, in some cases, present areas with relatively high local porosity. While the characteristics of the ITZ cannot be resolved, the detection of the aggregates' boundaries (and, therefore, of their shape) may help to identify siliceous grains within the cementitious matrix regardless of their similar linear attenuation coefficients, as visible in Figure 4. Generally, X-ray CT images of reinforced concrete specimens allow observing the status of the steel reinforcement and of the surrounding concrete, identifying the buildup of corrosion products, loss of steel cross-section due to corrosion and corrosion-induced cracks in the matrix [17-18], as visible in the examples reported in Figure 4.

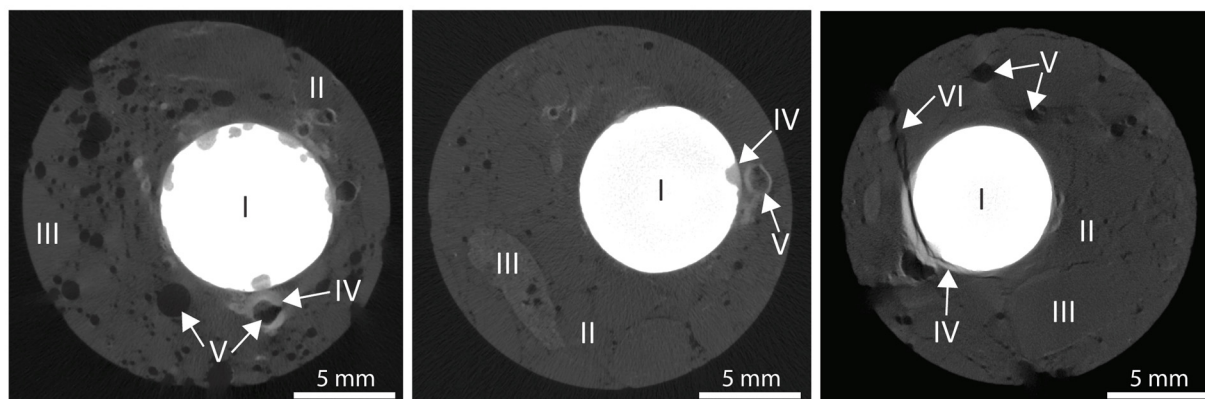


Figure 4. 2D cross sections of 20-year-old naturally corroded reinforced concrete specimens illustrating the different sample components: steel rebar (I), cementitious phases (II), aggregates (III), corrosion products (IV), voids (V), and cracks (VI). More information about the specimens can be found in Rossi et al. [17-18].

Already in the first applications of X-ray CT in reinforced concrete specimens [19-21], the relatively high attenuation coefficient of iron (and, generally, of heavy metals) gave the opportunity to clearly identify the reinforcement, observe the occurrence of corrosion attacks, and quantify the progressive development of the corrosion-induced damage. A significant number of studies have quantified the volume loss of steel due to corrosion [22-37] as well as measured the geometric characteristics of the corrosion sites (i.e., 2D cross-section loss) [17, 38]. Generally, the available studies on the topic had two main objectives: (i) to monitor the development of corrosion over time in terms of cross-sectional loss and consequent concrete cracking [21, 26-27, 29-31, 34, 36-42], as well as (ii) to study the distribution and transport of corrosion products in the surrounding concrete matrix [21, 25, 28-29, 32-33, 35-42]. In other cases, X-ray CT was applied to validate the results of corrosion initiation detection through acoustic emission [24] and to study the influence that interfacial defects have on corrosion initiation sites and buildup of corrosion product [17, 23].

Whilst the imaging potential of X-ray CT to study corrosion of steel in concrete has been widely confirmed by the studies available in the literature, similar X-ray linear attenuation coefficients of certain components of the specimens (e.g., sand grains and cementitious phases) and the low sensitivity of X-rays to light elements (such as hydrogen) are often considered as limitations of this technique. The former may hamper an accurate segmentation of the internal components of reinforced concrete specimens, which is fundamental to perform representative qualitative observations and reliable quantitative analyses. The latter is believed to hinder the detection of solution in cementitious materials, which is more deeply discussed in the next section. To overcome these limitations, recent studies investigated the applicability of bimodal imaging scanning, that is, acquiring volume scans of one specimen with X-rays and neutrons simultaneously (or consecutively) [43-45]. The reinforced concrete components have different ways of interacting with the incident X-rays and neutrons: while X-rays interact with the electron clouds of the atom and the X-rays attenuation coefficient of one element is directly proportional to its atomic number (Z),

neutrons interact with the nuclei of elements without getting attenuated depending on their atomic characteristics. Since hydrogen is highly neutron-attenuating, neutron CT also gives the possibility to image water transport, as already demonstrated in soil and cementitious materials [46-48]. Therefore, this methodology allows the characterization of the internal components of one specimen with much higher accuracy than that given by the separate CTs.

2.1 Observing solution with X-ray CT

The low sensitivity of X-rays to light elements may limit the detection of solution with standard X-ray CT due to the lack of contrast between the penetrating fluid and the surrounding matrix in the acquired images, especially in cementitious porous media because of their complex microscopic porosity network [10, 48-51]. For this reason, water transport in cementitious materials has been (successfully) studied with other methods such as, among others, performing multiple acquisitions over time and detecting the penetrating fluid front through arithmetic operations on the image stacks [52], X-ray dark-field imaging method to enhance the contrast between saturated and unsaturated portions of the specimen [53], and thanks to the application of contrast enhancers mixed within the exposure solution to track its movements within the cementitious pores [49-51]. While the latter method is generally not preferred since the contrast agent may influence the properties of the solution and may react with the porous material, the former methods require multiple (at least two) acquisitions to detect fluid ingress which is generally obtained by subtracting the image stack of the specimen under dry (controlled) conditions from that of the specimen undergoing water penetration. In one single acquisition, distinguishing between portions of the specimen that have a different degree of saturation may not be possible due to the relatively low X-ray linear attenuation coefficient of water [50]. The aim of this letter is to clarify, however, that the detection of solution in porous media through X-rays is not a limitation per se, but depends on the size of the pores (i.e., the porous volume in which the can solution penetrate)

relative to the spatial resolution of the performed acquisitions.

Before further discussing the feasibility of observing solution within cementitious materials, it is worth mentioning that as water penetrates the porous network of cementitious materials, the dissolution of hydrate phases (at varying rates) may result in changes in the chemistry and an increase in the ionic strength of the pore solution. Cement composition, hydration time, initial pore solution chemistry, among other chemical and engineering parameters, influence the dissolution rate of hydrate phases and consequentially, both the composition and ionic strength of the penetrating fluid [54-55]. Therefore, the penetrating fluid may have different X-ray attenuation properties, when compared to pure water. However, for the sake of simplicity, the linear attenuation coefficient of the fluid penetrating the cementitious materials (to which we refer as "solution" in this manuscript) will be herein considered as equal to that of pure water due to the relatively low concentrations of other elements. Furthermore, the influence of the beam-hardening effects and of the type and thickness of the material analyzed on the effective linear attenuation coefficient of the solution [8, 56] will be neglected, since the voxel object of the analysis reported later in this study (Figure 7) is considered under ideal conditions (i.e., isolated from the surroundings and therefore not influenced by the variations of the incident energy spectrum). In this way, the (relative) linear coefficient variations are estimated based on the different porosities and degrees of saturation only.

The linear attenuation coefficient of the solution penetrating the cementitious matrix due to exposure to wet-dry cycles or continuous submersion (as well as that of solution with a relatively small concentration of other elements such as NaCl solution simulating seawater) can be considered to be 103 times higher than that of air (Figure 3). Hence, empty pores (i.e., filled by dry air) have a significantly different (lower) attenuation than that of pores filled with solution. Nevertheless, capillary pores have dimensions ranging between 10 nm and 1 μm , which are significantly lower than the minimum voxel size of X-ray CT acquisitions performed on reinforced concrete specimens [23] according to the literature, as visible in Figure 5.

To distinguish capillary pores with X-ray CT, the spatial resolution of the acquisition must be at least in the range of the dimensions of the pores. Improving the spatial resolution of the acquired images is however (generally) not feasible when studying specimens with realistic geometric characteristics (i.e., size), with representative elementary volume and pore space morphology. As visible in Figure 6a, the majority of the studies report on X-ray CT acquisitions on specimens with a cementitious cover ranging between 2 and 20 mm and a reinforcement diameter of 2 to 10 mm, resulting in a voxel size of the acquired images of 5-50 μm . Even in the studies where the geometric characteristics of the specimens have been reduced to a few mm, the voxel size of the output image was not lower than around 3 μm [23, 28]. Improving further the spatial resolution of these acquisitions is limited by the minimum thickness and density that reinforced

cementitious specimens have, which in turn influences the optimum X-ray energy at which the acquisition is performed. Generally, relatively high X-ray energies (e.g., 150 keV and above) are needed to penetrate heavy metals (such as steel) [9], while moderate energies in the range of 50-150 keV are suitable for ceramic materials. The higher the thickness and density of the specimen, the higher the optimal X-ray source energy to penetrate the tested material, as suggested by the relation between acceleration voltages used and the geometric characteristics of the specimens analyzed in the literature of X-ray CT on reinforced cementitious materials [17, 19-45, 58] (Figure 6b).

When observing cementitious materials through X-ray CT with a voxel size higher than the dimensions of the different separate phases, each voxel representative of the cementitious matrix is imaged as a cluster that includes mainly hydrated cementitious phases (C-S-H and CH), unhydrated cement particles, and (capillary) pores. While some characteristics and components of the specimen can be in the range on nanometers (e.g., capillary pores, for instance), the imaged cluster cannot be obviously smaller than the voxel size of the acquired X-ray image. The volume of solution that can be absorbed by the cement matrix cluster is equal, under saturated conditions, to the volume of the pores. In completely dry conditions, on the other hand, the capillary porosity would be filled by dry air. This latter scenario is, however, very unlikely as there will always be a certain amount of pore solution in the capillary pores of the cementitious matrix under ordinary conditions. Due to the relatively low volume fraction of capillary pores in the cementitious matrix [57], X-ray images of the cement matrix under dry or saturated conditions do not show appreciable differences. The theoretical linear attenuation coefficient of one voxel representative of the cementitious matrix (μ_{matrix}) has been calculated for different ideal configurations of capillary porosity (5-20%) and degree of saturation (0- 100%) according to Equation (2) and as shown in Figure 7:

$$\mu_{\text{matrix}} = (\mu_{\text{hp}} \times V_{\text{hp}}) + (\mu_{\text{H}_2\text{O}} \times V_{\text{pores}} \times DoS) + (\mu_{\text{Air}} \times V_{\text{pores}} \times (1 - DoS)) \quad (2)$$

where μ_{hp} , $\mu_{\text{H}_2\text{O}}$ and μ_{Air} are the linear attenuation coefficients (cm^{-1}) of cement hydrate phases water and dry air, respectively; V_{hp} is the volume fraction of cementitious hydrate phases for the considered configurations (80-95%); V_{pores} is the volume fraction of total capillary porosity for the considered configurations (5-20%); DoS is the degree of saturation of the capillary pores (%), that is, the ratio between the volume of solution filling the pores (V_{solution}) and the volume fraction of the total capillary porosity (V_{pores}). The linear attenuation coefficients used in the present calculation are considered constant and correspond to an electron acceleration voltage of 60 keV, which is the highest intensity peak of X-ray spectra of a typical laboratory source at 150 keV (Figure 3b). The same acceleration voltage has also been used in the X-ray CT acquisitions reported later in this manuscript.

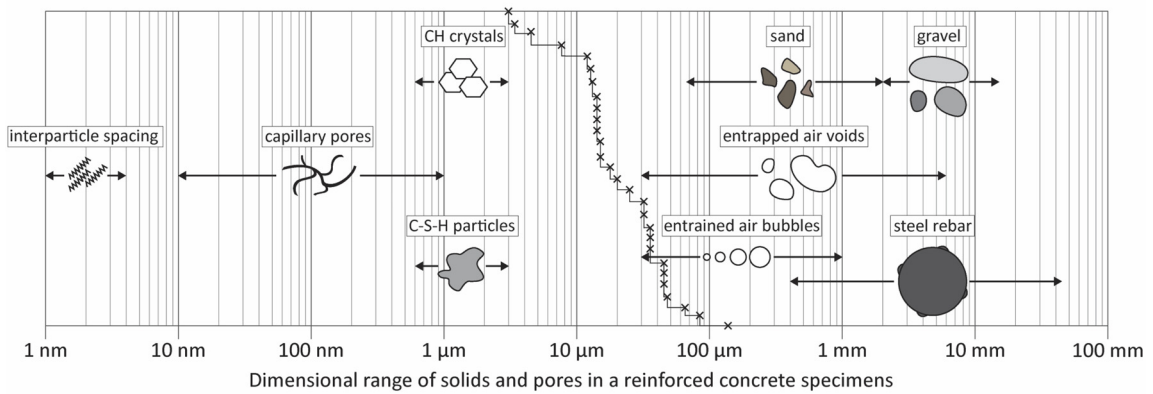


Figure 5. Size range of the different phases typically found in reinforced concrete specimens (inspired by [57]). Crosses (x) indicate the different pixel/voxel sizes of the X-ray CT acquisitions performed to study corrosion of steel in concrete available in the literature (lowest voxel size= 3.01 μm [23]; highest voxel size=140 μm [58]). (The lowest dimensions of entrained and entrapped air voids are based on the authors’ observations of X-ray CT acquisitions of cementitious materials; voids with smaller dimensions may also be present but not observed due to limitations of the image spatial resolution).

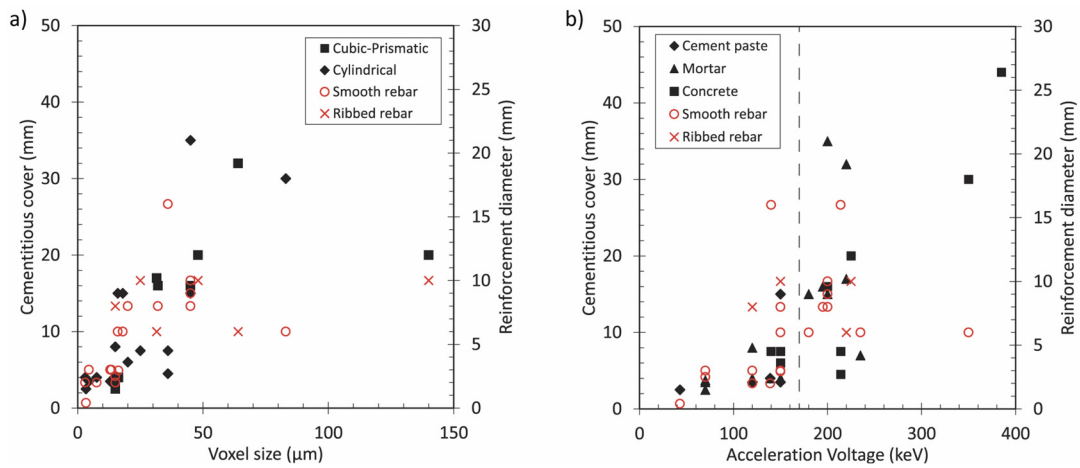


Figure 6. (a) Voxel size and (b) acceleration voltage at the source in relation to the cementitious cover and reinforcement diameter of the specimens as reported in the literature of X-ray CT acquisitions conducted to study corrosion of steel in concrete [17, 19-45, 58] (black-solid symbols refer to the primary vertical axis, while non-filled red symbols refer to the secondary vertical axis). The dotted vertical line in (b) indicates the average electron acceleration voltage among the available studies.

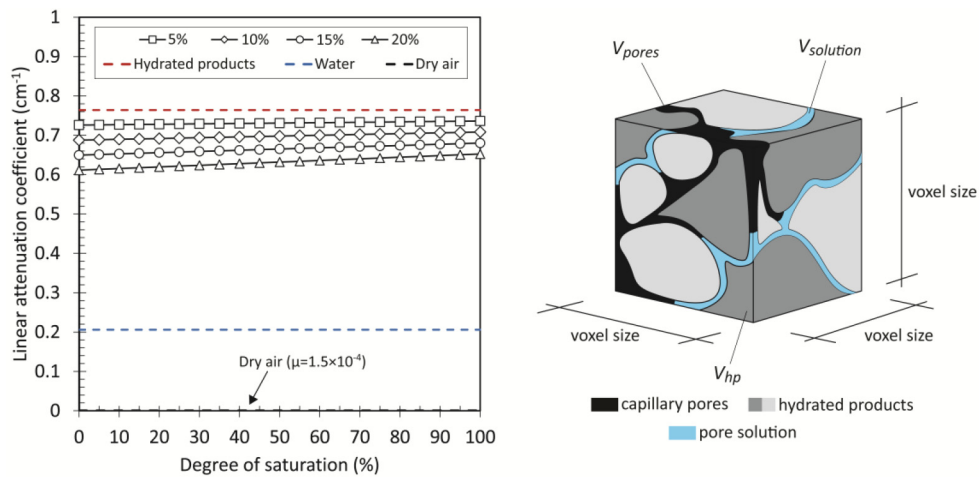


Figure 7. Calculation of μ_{matrix} of an ideal voxel representative of the cementitious matrix with different volume fractions of cement hydration products, namely CH and C-S-H (80-95%), porosity (5-20%) and DoS (0-100%). The ideal voxel considered in the computation is schematically represented on the right of the figure. The linear attenuation coefficients of hydrated products, water and dry air correspond to an electron acceleration voltage of 60 keV. The results of this estimation are relative to the used configuration only and not considering the influence that beam-hardening, material type and thickness may have on the obtained values.

As visible in Figure 7, the linear attenuation coefficient of the ideal voxel representative of the hydrated cementitious cluster does not considerably vary in relation to its estimated porosity and its degree of saturation. The highest deviation from μ_{hp} , of roughly 20%, corresponds to the cluster configuration with the highest porosity (e.g., 20%) and the lowest DoS (e.g., 0%). However, for more realistic scenarios where DoS \geq 50%, these variations are not larger than 14%.

The phases detected with X-ray CT do not have a singular characteristic GSV, but an interval of the GSV histogram [34, 38], which is used to perform segmentation of the internal components. In this context, the relatively small variations in μ_{matrix} with different porosity and DoS may hinder the possibility of clearly detecting the presence and transport of solution in capillary pores [50], at least not without prior calibration of the linear attenuation coefficient of the matrix under completely dry and saturated conditions [59]. For example, Michel and Pease [52] studied the ingress of moisture in cracked cementitious materials through X-ray attenuation measurements without using contrast enhancer agents. In their study, the effective linear attenuation coefficient of the solution penetrating in the porous network was considered, that is, including the influence of the type of material in which solution penetrates as well as of its thickness [56]. In so doing, the moisture ingress front in the porous network could be observed over time, proving that the increase in the linear attenuation coefficient of the composite material due to water uptake only could be detected. Nevertheless, the results of the moisture content within the pores (obtained by logarithmically subtracting the X-ray photons passing through an initially dry specimen to the beam passing through the same specimen under wet conditions) were subjected to significant variability (according to the authors' discussion). It is also worth mentioning that observing the moisture ingress front as conducted in their study required several measurements over time at relatively short time intervals (e.g., in the range of hours), and that the measured X-ray attenuation must also be considered as an average within the specimen thickness. Similar considerations apply to the results reported by Yang et al. [53], who could observe water uptake in capillary pores of mortar specimens through X-ray dark-field radiographs. Frequent acquisitions and, therefore, the detection of the moisture ingress front with the same methodology is generally not applicable in X-ray CT given the water desorption that may occur during the relatively high exposure time that specimens require to be tested, which is one of the key factors to have a 3D overview of the internal status of the specimen as output. While fast X-ray CT scans may overcome this limitation, the accuracy of the results may get compromised by the increased noise of the acquisition [60].

Different considerations arise when considering the presence of solution in larger porous networks, such as in coarse air voids within the concrete matrix. Air voids can be clearly distinguished inside the specimen volume on the basis of the low X-ray attenuation coefficient of dry air (Figure 3) and the dimensions of voids, which range from a few μm to several mm (Figure 4). The possibility to observe free solution in air

voids depends on, among other factors, the signal-to-noise ratio (SNR) of the acquisitions. The SNR is the ratio between the actual X-ray signal and its fluctuation, and it corresponds to how clearly the internal components of one specimen can be distinguished. With an adequate SNR (which can be improved by increasing the exposure time of the acquisitions) the difference between the attenuation of air and solution gives the possibility to observe the latter within voids when present. Observing solution when localized in very large (mm-scale) pores using X-ray CT was already mentioned by Yang et al. [53] and shown in water-saturated mortar specimens [61]. It is worth mentioning, however, that in their study a synchrotron radiation X-ray CT was used, which provides a monochromatic X-ray beam with higher flux and intensity compared to standard X-ray CT. With synchrotron radiation X-ray CT, the SNR as well as the spatial resolution of the acquired images are significantly improved, as in Yang et al.'s work where images with a pixel size of 1.28 μm performed at 55 keV were obtained [61]. Similar characteristics cannot be generally obtained through standard X-ray CT setups, which are usually more available in laboratories and, therefore, more widely used. Furthermore, the effectiveness of grating interferometry phase contrast imaging may be limited when testing highly contrasting materials like reinforced concrete, primarily due to the significant differences in the phase coefficients of the steel and the cementitious phases. Even though this technique offers unique advantages in enhancing image contrast for observing moisture transport in certain scenarios, such as in mortar samples, its application may be more limited in the context of steel-reinforced concrete.

As a matter of fact, the presence of water in air voids (in the range of mm) with standard X-ray CT has though been only scarcely studied [62], and never before in air voids at the steel-concrete interface (SCI) of reinforced cementitious specimens. Nevertheless, the results of this study show that conventional X-ray CT not only provides a practical, representative, and accessible means to image such reinforced cementitious materials, but also excels in capturing critical aspects like water or pore solutions in the macro-pores (e.g., air voids) at the SCI, making it a more suitable choice for studying the combined influence that interfacial defects and their moisture conditions have on the mechanism of steel corrosion. To confirm this fact, a set of X-ray CT images of one reinforced mortar specimen is visible in Figure 8. The reinforced mortar specimen was made with mixing proportions of 2:5 of Ordinary Portland cement (OPC) and aggregates ($D_{\text{max}} = 2 \text{ mm}$), respectively, and a water-cement ratio of 0.45. The diameter of the mortar cylinder was 20 mm, in which a smooth carbon steel rebar with an external diameter of 6 mm is centrally embedded, resulting in a cover depth of 7 mm. One initial acquisition of the specimen was performed in its dry state after 28 days of hydration at RH>95% and 20°C (Figure 8a-b). After that, the specimen was kept submerged in 3.5 wt.% NaCl solution and imaged after 8 weeks (Figure 8c) and 14 weeks of submersion (Figure 8d). The acquisitions at 8 and 14 weeks of exposure (Figure 8c-d) were conducted after taking the sample out of the exposure solution and wrapping it with parafilm just before each X-ray CT acquisition. The X-ray CT acquisitions were conducted at

the ICON beamline of Paul Scherrer Institute (PSI, Villigen, Switzerland) [63], with an acceleration voltage of 150 keV to acquire 1125 projections over 360° of rotation, each one with an exposure time of 20 seconds. The reconstruction of the X-ray CT acquisitions was performed using MuhRec [64]. The outcome of each reconstruction was a stack of 2175 images with 1791×1791 pixels (16 bits) per image, with a final voxel size of 13.8 μm .

The X-ray CT cross-sections depicted in Figure 8b-d show the ingress of solution in an air void at the SCI at three points in time. The magnified interfacial void is completely solution-free after cement hydration (i.e., 28 days after casting, Figure 8b), while it gets progressively filled by solution after 8 weeks (Figure 8c) and 14 weeks (Figure 8d) of submersion in NaCl solution. The contact angle of the gas-liquid interface is clearly visible after submersion in solution (Figure 8c-d), in line with other studies that elaborated on the evolution of DoS in the air void-shell system in cementitious materials under submerged conditions [65]. After both 8 and 14 weeks of submersion (Figure 8c-d), the air void is partially filled by solution while the gaseous phase volume shrinks over time in a single bubble in contact with the steel reinforcement.

To the best of our knowledge, X-ray CT observations detailing the presence of solution within air voids at the SCI of reinforced cementitious materials have not been previously documented in the literature. Among other reasons, the lack of these data could be due to the fact that most of the X-ray CT acquisitions of reinforced concrete specimens shown by other studies have been conducted during the drying phase of solution wet-dry cycles [25, 32-33, 35-36, 40, 42, 66] or specimens were dried out in an oven or at room temperature to reduce any potential inaccuracies related to the presence of solution inside the specimens during the acquisitions [17, 31, 45]. Rarely, the specimens were kept wrapped during the X-ray CT acquisitions to maintain their internal moisture conditions [34], which however did not report any observation of solution in air voids, most likely because corrosion of steel reinforcement was accelerated with impressed current keeping the specimens in a humidity chamber and not continuously submerged in solution. In most of the other studies in the literature, it was not specified if the moisture conditions of the specimens were preserved [26, 30, 38-39, 41, 44, 58, 67-68].

It is out of the scope of the present letter to elaborate on the mechanism through which air voids get filled by solution, which would require more quantitative and statistical analysis on, for instance, more specimens and the saturation degree of their voids over time, also depending on their exposure conditions. More analysis in this regard will therefore be conducted in future studies. Nevertheless, the qualitative observations herein reported confirm that the presence of solution in macro-pores or coarse air voids may be more deeply and quantitatively studied through X-ray CT, which is of fundamental relevance to elucidate the role that interfacial air voids and their moisture conditions have on several degradation mechanisms of reinforced concrete structures, such as steel corrosion and freeze-thaw damage. The former topic has been comprehensively discussed by the RILEM TC 262-SCI [69], which hypothesized that partially or completely filled interfacial voids may create the ideal conditions for corrosion to onset in a chloride-contaminated environment. When interfacial voids are completely saturated, the area of steel directly exposed to the solution would be more prone to corrosion than the areas covered with cement paste since the CH-rich matrix would locally buffer the pH during early pitting. Interfacial air voids partially filled with solution are considered the worst-case scenario for corrosion resistance, since the simultaneous presence of electrolyte and oxygen in direct contact with the steel surface would aggravate the corrosion initiation process. On the contrary, when interfacial voids are air-filled (e.g., in dry conditions), the steel reinforcement is expected to be covered by a thin layer of absorbed water only, which would drastically reduce the transport of aggressive ions (e.g., chlorides) to the steel area. The portion of steel in direct contact with an interfacial void would likely not be the most sensitive location for corrosion initiation in this scenario. Nevertheless, air-filled interfacial voids may act as an oxygen "reservoir" to sustain the cathodic reaction that may stabilize corrosion attacks in its proximity, hence promoting corrosion initiation at adjacent areas. Even though these hypotheses could explain the strong dependency of steel corrosion initiation on the moisture state of interfacial air voids, experimental evidence of these theories is still lacking.

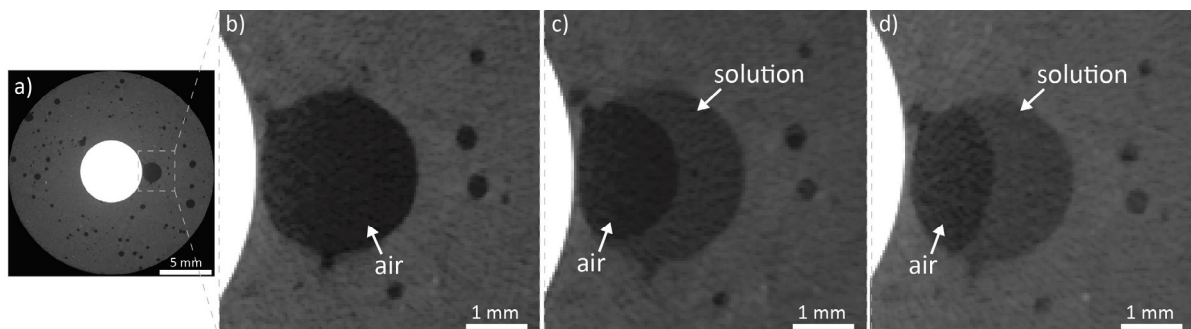


Figure 8. X-ray CT cross-sections of one reinforced mortar cylindrical specimen showing water ingress in interfacial voids over time; a) specimen overview in its dry conditions after 28 days of hydration; b) magnified interfacial air void in dry conditions; c) magnified interfacial air void after 8 weeks of submersion in NaCl solution; d) magnified interfacial air void after 12 weeks of submersion in NaCl solution. In the magnified areas, the detected solution is indicated by white arrows.

According to the results of the present study, we believe that further research through X-ray CT has the potential to elucidate the impact of the moisture state of macroscopic interfacial concrete voids on corrosion initiation. Similarly, settlement and bleeding zones formed during concrete casting may be air-filled or (partly) solution-filled depending on their exposure conditions [70]. The occurrence of these defects may affect both the steel-concrete bond properties and the steel susceptibility to corrosion onset. Nevertheless, only limited data on the influence of their moisture conditions of corrosion initiation is available in the literature [69], which may therefore benefit from the application of the findings herein reported in future research. In principle, the precipitation of corrosion products at the SCI and their transport in the matrix in relation to the local moisture conditions could also be studied through X-ray CT, which may give further insights about the penetration of corrosion products into the surrounding concrete and the stresses induced by the corrosion products buildup. Nevertheless, it is important to bear in mind the limitations of X-ray CT given by its highest spatial resolution (in the range of μm under standard conditions), which therefore generally exclude the possibility of resolving nano- or micro-scale mechanisms such as, for instance, phase transformation of iron (hydr)oxides.

The same methodology may also contribute to studying the evolution of the DoS of air voids in the bulk concrete matrix over time and depending on the surrounding exposure conditions. The DoS of concrete air voids is a crucial parameter to assess the freezing-thawing resistance of the mixture since damage due to freeze-thaw occurs when concrete exceeds its critical saturation threshold (DoS_{CR}) as a function of its air-pore system [71-72]. Even though other studies already focused on studying fluid absorption in capillary pores and air voids through neutron radiography and X-ray CT with contrast-enhancing agents [51, 59], the detection of solution in air voids with X-ray CT as reported in the present letter may contribute even further to improve the current knowledge of the mechanism of freeze-thaw damage in cementitious materials, as rarely attempted [73].

3 Conclusions and future perspectives

This study reports on the application of X-ray CT to observe the presence of solution in air voids at the SCI of cementitious materials. The qualitative results of this study show that the longer the submersion in solution, the higher the decrease of gas volume within an interfacial air void, which clusters in one single air bubble in the case reported herein.

It is worth mentioning that the DoS of concrete air voids is a key parameter for several degradation mechanisms of reinforced concrete. For instance, the steel reinforcement sensitivity to corrosion onset has been reported to be highly influenced by the presence of interfacial defects and, even more importantly, by their moisture conditions. The moisture conditions of air voids may also influence the mechanisms of corrosion product precipitation and buildup at the SCI as well as the resistance of cementitious materials to freezing and thawing. Multiple research possibilities may result from the capability of X-ray CT to detect solution in concrete air voids

as shown in this study, which may significantly contribute to elucidating the impact of the moisture state of macroscopic voids on (reinforced) concrete durability issues.

Acknowledgments

This work was supported by the Swiss National Science Foundation [project no. CRSII5_205883], which is deeply acknowledged.

Authorship statement (CRediT)

Emanuele Rossi: Conceptualization, Methodology, Formal analysis, Investigation, Visualization, Writing – original draft. **Susanna Governo:** Investigation, Writing – review and editing. **Mahdieh Shakoorioskooie:** Investigation, Writing – review and editing. **Qianru Zhan:** Writing – review and editing. **Shishir Mundra:** Writing – review and editing, Supervision. **David Mannes:** Writing – review and editing. **Anders Kaestner:** Writing – review and editing, Supervision. **Ueli Angst:** Conceptualization, Methodology, Writing – review and editing, Supervision, Project administration, Funding acquisition.

References

- [1] S. A. Miller, A. Horvath, P. J. Monteiro, Readily implementable techniques can cut annual CO₂ emissions from the production of concrete by over 20%, *Environmental Research Letters* (2016), 11(7), 074029. <https://doi.org/10.1088/1748-9326/11/7/074029>
- [2] K. L. Scrivener, V. M. John, E. M. Gartner, Eco-efficient cements: Potential economically viable solutions for a low-CO₂ cement-based materials industry, *Cement and Concrete Research* (2018), 114, 2-26. <https://doi.org/10.1016/j.cemconres.2018.03.015>
- [3] A. E. K. Jones, Development of an holistic approach to ensure the durability of new concrete construction, *British Cement Association* (1997).
- [4] U. M. Angst, Steel corrosion in concrete-Achilles' heel for sustainable concrete? *Cement and Concrete Research* (2023), 172, 107239. <https://doi.org/10.1016/j.cemconres.2023.107239>
- [5] H. S. Wong, U. M. Angst, M. R. Geiker, O. B. Isgor, B. Elsener, A. Michel, M. C. Alonso, M. J. Correia, J. Pacheco, J. Gulikers, Y. Zhao, M. Criado, M. Raupach, H. Spørensens, R. François, S. Mundra, M. Rasol, R. Polder, Methods for characterising the steel-concrete interface to enhance understanding of reinforcement corrosion: a critical review by RILEM TC 262-SCI, *Materials and structures* (2022), 55(4), 124. <https://doi.org/10.1617/s11527-022-01961-5>
- [6] R. A. Ketcham, W. D. Carlson, Acquisition, optimization and interpretation of X-ray computed tomographic imagery: applications to the geosciences, *Computers & Geosciences* (2001), 27(4), 381-400. [https://doi.org/10.1016/S0098-3004\(00\)00116-3](https://doi.org/10.1016/S0098-3004(00)00116-3)
- [7] V. Cnudde, M. N. Boone, High-resolution X-ray computed tomography in geosciences: A review of the current technology and applications, *Earth-Science Reviews* (2013), 123, 1-17. <https://doi.org/10.1016/j.earscirev.2013.04.003>
- [8] S. Roels, J. Carmeliet, Analysis of moisture flow in porous materials using microfocus X-ray radiography, *International Journal of Heat and Mass Transfer* (2006), 49(25-26), 4762-4772. <https://doi.org/10.1016/j.ijheatmasstransfer.2006.06.035>
- [9] R. D. Hanna, R. A. Ketcham, X-ray computed tomography of planetary materials: A primer and review of recent studies, *Geochemistry* (2017), 77(4), 547-572. <https://doi.org/10.1016/j.chemer.2017.01.006>
- [10] S. Brisard, M. Serdar, P. J. Monteiro, Multiscale X-ray tomography of cementitious materials: A review, *Cement and Concrete Research* (2020), 128, 105824. <https://doi.org/10.1016/j.cemconres.2019.105824>
- [11] M. Alhusain, A. Al-Mayah, Three-dimensional imaging of reinforcement corrosion using micro-computed tomography: Literature review, *Construction and Building Materials* (2021), 284, 122813. <https://doi.org/10.1016/j.conbuildmat.2021.122813>

- [12] T. M. Buzug, Computed tomography, Springer handbook of medical technology (2011), 311-342, Berlin, Heidelberg: Springer Berlin Heidelberg. https://doi.org/10.1007/978-3-540-74658-4_16
- [13] J. H. Hubbell, S. M. Seltzer, NIST standard reference database 126. Gaithersburg, MD: National Institute of Standards and Technology (1996), <https://dx.doi.org/10.18434/T4D01F>
- [14] G. Poludniowski, P. M. Evans, Calculation of X - ray spectra emerging from an X - ray tube. Part I. Electron penetration characteristics in X - ray targets, Medical physics (2007), 34(6Part1), 2164-2174. <https://doi.org/10.1118/1.2734725>
- [15] G. Poludniowski, Calculation of X - ray spectra emerging from an X - ray tube. Part II. X - ray production and filtration in X - ray targets, Medical physics (2007), 34(6Part1), 2175-2186. <https://doi.org/10.1118/1.2734726>
- [16] G. Poludniowski, G. Landry, F. Deblois, P. M. Evans, F. Verhaegen, SpekCalc: a program to calculate photon spectra from tungsten anode X-ray tubes, Physics in Medicine & Biology (2009), 54(19), N433. <https://doi.org/10.1088/0031-9155/54/19/N01>
- [17] E. Rossi, R. Polder, O. Copuroglu, T. Nijland, B. Šavija, The influence of defects at the steel/concrete interface for chloride-induced pitting corrosion of naturally-deteriorated 20-years-old specimens studied through X-ray Computed Tomography, Construction and Building Materials (2020), 235, 117474. <https://doi.org/10.1016/j.conbuildmat.2019.117474>
- [18] E. Rossi, H. Zhang, S. J. Garcia, J. Bijleveld, T. G. Nijland, O. Copuroglu, R. Polder, B. Šavija, Analysis of naturally-generated corrosion products due to chlorides in 20-year old reinforced concrete: An elastic modulus-mineralogy characterization, Corrosion Science (2021), 184, 109356. <https://doi.org/10.1016/j.corsci.2021.109356>
- [19] M. Beck, J. Goebbels, A. Burkert, Application of X - ray tomography for the verification of corrosion processes in chloride contaminated mortar, Materials and Corrosion (2007), 58(3), 207-210. <https://doi.org/10.1002/maco.200604049>
- [20] M. Beck, J. Goebbels, A. Burkert, B. Isecke, R. Bäßler, Monitoring of corrosion processes in chloride contaminated mortar by electrochemical measurements and X - ray tomography, Materials and Corrosion (2010), 61(6), 475-479. <https://doi.org/10.1002/maco.200905364>
- [21] D. Neff, J. Harnisch, M. Beck, V. L'Hostis, J. Goebbels, D. Meinel, Morphology of corrosion products of steel in concrete under macro - cell and self - corrosion conditions, Materials and Corrosion (2011), 62(9), 861-871. <https://doi.org/10.1002/maco.201005861>
- [22] A. Česen, T. Kosec, A. Legat, Characterization of steel corrosion in mortar by various electrochemical and physical techniques, Corrosion Science (2013), 75, 47-57. <https://doi.org/10.1016/j.corsci.2013.05.015>
- [23] X. Zhang, G. Zuo, S. A. Memon, F. Xing, H. Sun, Effects of initial defects within mortar cover on corrosion of steel and cracking of cover using X-ray computed tomography, Construction and Building Materials (2019), 223, 265-277. <https://doi.org/10.1016/j.conbuildmat.2019.06.172>
- [24] C. Van Steen, L. Pahlavan, M. Wevers, E. Verstrynghe, Localisation and characterisation of corrosion damage in reinforced concrete by means of acoustic emission and X-ray computed tomography, Construction and Building Materials (2019), 197, 21-29. <https://doi.org/10.1016/j.conbuildmat.2018.11.159>
- [25] F. Bernachy-Barbe, T. Sayari, V. Dewynter-Martyn, V. L'Hostis, Using X-ray microtomography to study the initiation of chloride-induced reinforcement corrosion in cracked concrete, Construction and Building Materials (2020), 259, 119574. <https://doi.org/10.1016/j.conbuildmat.2020.119574>
- [26] F. de Mendonça Filho, O. Copuroglu, E. Schlangen, B. Šavija, Determination of loss of reinforcement due to corrosion through X-ray computer micro-tomography, Materials (2021), 14(4), 893. <https://doi.org/10.3390/ma14040893>
- [27] S. Hong, F. Zheng, G. Shi, B. Dong, M. Liu, L. Tang, Y. Zhang, Determining influence of impressed current density on current efficiency with X-ray micro-computed tomography, Construction and Building Materials (2020), 246, 118505. <https://doi.org/10.1016/j.conbuildmat.2020.118505>
- [28] P. A. Itty, M. Serdar, C. Meral, D. Parkinson, A. A. MacDowell, D. Bjegović, P. J. Monteiro, In situ 3D monitoring of corrosion on carbon steel and ferritic stainless steel embedded in cement paste, Corrosion Science (2014), 83, 409-418. <https://doi.org/10.1016/j.corsci.2014.03.010>
- [29] S. Hong, G. Shi, F. Zheng, M. Liu, D. Hou, B. Dong, Characterization of the corrosion profiles of reinforcement with different impressed current densities by X-ray micro-computed tomography, Cement and Concrete Composites (2020), 109, 103583. <https://doi.org/10.1016/j.cemconcomp.2020.103583>
- [30] G. Ebell, A. Burkert, J. Fischer, J. Lehmann, T. Müller, D. Meinel, O. Paetsch, Investigation of chloride - induced pitting corrosion of steel in concrete with innovative methods, Materials and Corrosion (2016), 67(6), 583-590. <https://doi.org/10.1002/maco.201608969>
- [31] B. Dong, G. Fang, Y. Liu, P. Dong, J. Zhang, F. Xing, S. Hong, Monitoring reinforcement corrosion and corrosion-induced cracking by X-ray microcomputed tomography method, Cement and Concrete Research (2017), 100, 311-321. <https://doi.org/10.1016/j.cemconres.2017.07.009>
- [32] B. Dong, W. Ding, S. Qin, G. Fang, Y. Liu, P. Dong, S. Han, F. Xing, S. Hong, 3D visualized tracing of rebar corrosion-inhibiting features in concrete with a novel chemical self-healing system, Construction and Building Materials (2018), 168, 11-20. <https://doi.org/10.1016/j.conbuildmat.2018.02.094>
- [33] B. Dong, W. Ding, S. Qin, N. Han, G. Fang, Y. Liu, F. Xing, S. Hong, Chemical self-healing system with novel microcapsules for corrosion inhibition of rebar in concrete, Cement and Concrete Composites (2018), 85, 83-91. <https://doi.org/10.1016/j.cemconcomp.2017.09.012>
- [34] S. Hong, F. Zheng, G. Shi, J. Li, X. Luo, F. Xing, L. Tang, B. Dong, Determination of impressed current efficiency during accelerated corrosion of reinforcement, Cement and Concrete Composites (2020), 108, 103536. <https://doi.org/10.1016/j.cemconcomp.2020.103536>
- [35] S. Hong, S. Qin, P. Dong, G. Li, Y. Zhang, F. Xing, B. Dong, Quantification of rust penetration profile in reinforced concrete deduced by inverse modeling, Cement and Concrete Composites (2020), 111, 103622. <https://doi.org/10.1016/j.cemconcomp.2020.103622>
- [36] G. Fang, W. Ding, Y. Liu, J. Zhang, F. Xing, B. Dong, Identification of corrosion products and 3D distribution in reinforced concrete using X-ray micro-computed tomography, Construction and Building Materials (2019), 207, 304-315. <https://doi.org/10.1016/j.conbuildmat.2019.02.133>
- [37] P. Wang, H. Qiao, Y. Zhang, Y. Li, K. Chen, Q. Feng, Three-dimensional characteristics of steel corrosion and corrosion-induced cracks in magnesium oxychloride cement concrete monitored by X-ray computed tomography, Construction and Building Materials (2020), 246, 118504. <https://doi.org/10.1016/j.conbuildmat.2020.118504>
- [38] H. Sun, D. Zhao, Y. Gu, S. A. Memon, Z. Ren, B. Liu, D. Li, Three-dimensional characterization of steel corrosion embedded in cement paste, Construction and Building Materials (2017), 143, 24-32. <https://doi.org/10.1016/j.conbuildmat.2017.03.106>
- [39] B. Šavija, M. Luković, S. A. S. Hosseini, J. Pacheco, E. Schlangen, Corrosion induced cover cracking studied by X-ray computed tomography, nanoindentation, and energy dispersive X-ray spectrometry (EDS), Materials and Structures (2015), 48, 2043-2062. <https://doi.org/10.1617/s11527-014-0292-9>
- [40] X. Xi, S. Yang, Investigating the spatial development of corrosion of corner-located steel bar in concrete by X-ray computed tomography, Construction and Building Materials (2019), 221, 177-189. <https://doi.org/10.1016/j.conbuildmat.2019.06.023>
- [41] J. Shi, J. Ming, Y. Zhang, J. Jiang, Corrosion products and corrosion-induced cracks of low-alloy steel and low-carbon steel in concrete, Cement and Concrete Composites (2018), 88, 121-129. <https://doi.org/10.1016/j.cemconcomp.2018.02.002>
- [42] B. Dong, G. Shi, P. Dong, W. Ding, X. Teng, S. Qin, J. Liu, F. Xing, S. Hong, Visualized tracing of rebar corrosion evolution in concrete with x-ray micro-computed tomography method, Cement and Concrete Composites (2018), 92, 102-109. <https://doi.org/10.1016/j.cemconcomp.2018.06.003>
- [43] U. M. Angst, E. Rossi, C. B. Käthler, D. Mannes, P. Trtik, B. Elsener, Z. Zhou, M. Strobl, Chloride-induced corrosion of steel in concrete—insights from bimodal neutron and X-ray microtomography combined with ex-situ microscopy, arXiv preprint arXiv:2307.10261 (2023).
- [44] S. Ribuschi, A. Tengattini, J. Dijkstra, I. Fernandez, K. Lundgren, A closer look at corrosion of steel reinforcement bars in concrete using 3D neutron and X-ray computed tomography, Cement and Concrete Research (2021), 144, 106439. <https://doi.org/10.1016/j.cemconres.2021.106439>

- [45] A. Alhede, J. Dijkstra, S. Robuschi, A. Tengattini, K. Lundgren, A two-stage study of steel corrosion and internal cracking revealed by multimodal tomography, *Construction and Building Materials* (2023), 394, 132187. <https://doi.org/10.1016/j.conbuildmat.2023.132187>
- [46] A. Tengattini, N. Lenoir, E. Ando, G. Viggiani, Neutron imaging for geomechanics: A review, *Geomechanics for Energy and the Environment* (2021), 27, 100206. <https://doi.org/10.1016/j.gete.2020.100206>
- [47] Z. Zhang, P. Trtik, F. Ren, T. Schmid, C. H. Dreimol, U. Angst, Dynamic effect of water penetration on steel corrosion in carbonated mortar: A neutron imaging, electrochemical, and modeling study, *Cement* (2022), 9, 100043. <https://doi.org/10.1016/j.cement.2022.100043>
- [48] M. A. Hickner, N. P. Siegel, K. S. Chen, D. S. Hussey, D. L. Jacobson, M. Arif, In situ high-resolution neutron radiography of cross-sectional liquid water profiles in proton exchange membrane fuel cells, *Journal of The Electrochemical Society* (2008), 155(4), B427. <https://doi.org/10.1149/1.2826287>
- [49] M. A. Boone, T. De Kock, T. Bultreys, G. De Schutter, P. Vontobel, L. Van Hoorebeke, V. Cnudde, 3D mapping of water in oolithic limestone at atmospheric and vacuum saturation using X-ray micro-CT differential imaging, *Materials Characterization* (2014), 97, 150-160. <https://doi.org/10.1016/j.matchar.2014.09.010>
- [50] L. Yang, Y. Zhang, Z. Liu, P. Zhao, C. Liu, In-situ tracking of water transport in cement paste using X-ray computed tomography combined with CsCl enhancing, *Materials Letters* (2015), 160, 381-383. <https://doi.org/10.1016/j.matlet.2015.08.011>
- [51] M. K. Moradillo, Q. Hu, M. T. Ley, Using X-ray imaging to investigate in-situ ion diffusion in cementitious materials, *Construction and Building Materials* (2017), 136, 88-98. <https://doi.org/10.1016/j.conbuildmat.2017.01.038>
- [52] A. Michel, B. J. Pease, Moisture ingress in cracked cementitious materials, *Cement and Concrete Research* (2018), 113, 154-168. <https://doi.org/10.1016/j.cemconres.2018.08.009>
- [53] F. Yang, F. Prade, M. Griffa, I. Jerjen, C. Di Bella, J. Herzen, A. Sarapata, F. Pfeiffer, P. Lura, Dark-field X-ray imaging of unsaturated water transport in porous materials, *Applied Physics Letters* (2014), 105(15). <https://doi.org/10.1063/1.4898783>
- [54] B. Lothenbach, F. Winnefeld, Thermodynamic modelling of the hydration of Portland cement, *Cement and Concrete Research* (2006), 36(2), 209-226. <https://doi.org/10.1016/j.cemconres.2005.03.001>
- [55] P. Lura, K. Friedemann, F. Stallmach, S. Mönig, M. Wyrzykowski, L. P. Esteves, Kinetics of water migration in cement-based systems containing superabsorbent polymers, Application of Super Absorbent Polymers (SAP) in Concrete Construction: State-of-the-Art Report Prepared by Technical Committee 225-SAP (2012), 21-37. https://doi.org/10.1007/978-94-007-2733-5_4
- [56] B. J. Pease, G. A. Scheffler, H. Janssen, Monitoring moisture movements in building materials using X-ray attenuation: Influence of beam-hardening of polychromatic X-ray photon beams, *Construction and Building Materials* (2012), 36, 419-429. <https://doi.org/10.1016/j.conbuildmat.2012.04.126>
- [57] P. K. Mehta, P. J. Monteiro, *Concrete: microstructure, properties, and materials*, McGraw-Hill Education (2014).
- [58] J. Shi, J. Ming, W. Sun, Accelerated corrosion behavior of steel in concrete subjected to sustained flexural loading using electrochemical methods and X-ray computed tomography, *Journal of Materials in Civil Engineering* (2018), 30(7), 04018131. [https://doi.org/10.1061/\(ASCE\)MT.1943-5533.0002337](https://doi.org/10.1061/(ASCE)MT.1943-5533.0002337)
- [59] M. K. Moradillo, C. Qiao, M. Keys, H. Hall, M. T. Ley, S. Reese, W. J. Weiss, Quantifying fluid absorption in air- entrained concrete using neutron radiography, *ACI Materials Journal* (2019), 116(6), 213-226. <https://doi.org/10.14359/51716980>
- [60] A. Du Plessis, B. J. Olawuyi, W. P. Boshoff, S. G. Le Roux, Simple and fast porosity analysis of concrete using X-ray computed tomography, *Materials and Structures* (2016), 49, 553-562. <https://doi.org/10.1617/s11527-014-0519-9>
- [61] F. Yang, Multi-contrast X-ray imaging of water transport in cement-based materials, Doctoral dissertation, ETH Zurich (2017).
- [62] D. Wahlbom, K. Fridh, Cryosuction Experiments on Concrete Containing Ground Granulated Blast-Furnace Slag: Influence of Temperature, Air Entrainment And Salt, *Nordic Concrete Research* (2023), 68(1), 1-15. <https://doi.org/10.2478/ncr-2022-0008>
- [63] A. P. Kaestner, J. Hovind, P. Boillat, C. Muehlebach, C. Carminati, M. Zarebanadkouki, E. H. Lehmann, Bimodal imaging at ICON using neutrons and X-rays, *Physics Procedia* (2017), 88, 314-321. <https://doi.org/10.1016/j.phpro.2017.06.043>
- [64] A. P. Kaestner, MuhRec-A new tomography reconstructor, *Nuclear Instruments and Methods in Physics Research Section A: Accelerators, Spectrometers, Detectors and Associated Equipment* (2011), 651(1), 156-160. <https://doi.org/10.1016/j.nima.2011.01.129>
- [65] S. H. Smith, M. Vandamme, K. E. Kurtis, Dissolution kinetics of trapped air in a spherical void: modeling the long-term saturation of cementitious materials, *Cement and Concrete Research* (2020), 130, 105996. <https://doi.org/10.1016/j.cemconres.2020.105996>
- [66] A. Rodríguez, S. Gutiérrez - González, M. I. Prieto, A. Cobo, V. Calderón, Analysis of long-term corrosion behavior in mortars containing recycled ladle furnace slag using computerized tomography and SEM, *Materials and Corrosion* (2015), 66(3), 199-205. <https://doi.org/10.1002/maco.201407697>
- [67] S. Erdem, X-ray computed tomography and fractal analysis for the evaluation of segregation resistance, strength response and accelerated corrosion behaviour of self-compacting lightweight concrete, *Construction and Building Materials* (2014), 61, 10-17. <https://doi.org/10.1016/j.conbuildmat.2014.02.070>
- [68] J. Shi, J. Ming, Influence of defects at the steel-mortar interface on the corrosion behavior of steel, *Construction and Building Materials* (2017), 136, 118-125. <https://doi.org/10.1016/j.conbuildmat.2017.01.007>
- [69] U. M. Angst, M. R. Geiker, M. C. Alonso, R. Polder, O. B. Isgor, B. Elsener, H. Wong, A. Michel, K. Hornbostel, C. Gehlen, R. François, M. Sanchez, M. Criado, H. Sørensen, C. Hansson, R. Pillai, S. Mundra, J. Hulikers, M. Raupach, J. Pacheco, A. Sagüés, The effect of the steel-concrete interface on chloride-induced corrosion initiation in concrete: a critical review by RILEM TC 262-SCI, *Materials and Structures* (2019), 52, 1-25. <https://doi.org/10.1617/s11527-019-1387-0>
- [70] U. M. Angst, M. R. Geiker, A. Michel, C. Gehlen, H. Wong, O. B. Isgor, B. Elsener, C. M. Hansson, R. François, K. Hornbostel, R. Polder, M. C. Alonso, M. Sanchez, M. J. Correia, M. Criado, A. Sagüés, N. Buenfeld, The steel-concrete interface. *Materials and Structures* (2017), 50, 1-24. <https://doi.org/10.1617/s11527-017-1010-1>
- [71] F. Fagerlund, The critical degree of saturation method of assessing the freeze/thaw resistance of concrete, *Matériaux et Construction* (1977), 10, 217-229. <https://doi.org/10.1007/BF02478693>
- [72] G. Fagerlund, Predicting the service life of concrete exposed to frost action through a modelling of the water absorption process in the air-pore system, In *The modelling of microstructure and its potential for studying transport properties and durability* (1996), 503-537, Dordrecht: Springer Netherlands. https://doi.org/10.1007/978-94-015-8646-7_28
- [73] D. Wahlbom, Moisture uptake and salt frost deterioration of concrete, Licentiate Thesis, Report TVBM - 3190, Division of Building Materials, Faculty of Engineering, Lund University (2022).